



COMPARATIVE STUDY OF COOLING STRATEGIES IN A LITHIUM-ION BATTERY MODULE FOR THERMAL RUNAWAY PREVENTION USING CFD

ESTUDIO COMPARATIVO DE ESTRATEGIAS DE ENFRIAMIENTO EN UN MÓDULO DE BATERÍAS DE IONES DE LITIO PARA LA PREVENCIÓN DE LA FUGA TÉRMICA MEDIANTE CFD

Ricardo Carpio-Chilloallo^{1,*} , Edwin Paccha-Herrera¹ 

Received: 16-08-2024, Received after review: 14-11-2024, Accepted: 26-11-2024, Published: 01-01-2025

Abstract

This study investigates the thermal behavior of three lithium-ion battery configurations under thermal runaway conditions, focusing on cooling systems based on air, water, and phase change materials (PCM). The analysis was conducted using sixteen cylindrical 18650 cells, each with a capacity of 2.15 Ah. The battery arrangements include Geometry 1, characterized by an irregular rhomboid shape, and Geometry 2, which adopts an irregular octagonal shape. Numerical simulations were carried out using Computational Fluid Dynamics (CFD) tools in ANSYS Fluent, employing a thermal abuse model rooted in a multidimensional, multiscale approach, and incorporating the empirical Newman-Tiedemann-Gauthier-Kim (NTGK) model. Transient simulations were performed under forced and natural convection scenarios to capture dynamic thermal behavior. The findings reveal that natural air cooling fails to prevent thermal runaway under the studied conditions. In contrast, water and PCM-based cooling systems effectively mitigate thermal runaway risks. Furthermore, forced convection with air and water significantly enhances thermal management and successfully prevents thermal runaway.

Keywords: Thermal abuse, ANSYS, cooling, NTGK, thermal runaway

Resumen

En este estudio se evalúa el comportamiento térmico ante condiciones de fuga térmica de tres arreglos de celdas de iones de litio con distintos sistemas de enfriamiento: aire, agua y material de cambio de fase (PCM). Se utilizaron 16 celdas cilíndricas de tipo 18650 con una capacidad de 2.15 Ah. La geometría 1 tiene una forma de rombo irregular, mientras que las geometrías 2 y 3 tienen una forma de un octágono irregular. Se implementaron simulaciones numéricas CFD empleando el software ANSYS Fluent mediante la aplicación del modelo de abuso térmico basado en un enfoque multidimensional multiescala y el modelo empírico NTGK. Se ejecutaron simulaciones transientes considerando convección forzada y natural. Los resultados muestran que, para las condiciones dadas en el estudio, el enfriamiento natural por aire no previene la fuga térmica, mientras que el agua y PCM sí la previenen, al igual que la convección forzada con aire y agua.

Palabras clave: abuso térmico, ANSYS, enfriamiento, NTGK, fuga térmica

^{1,*}Universidad Nacional de Loja, Loja, Ecuador.
Corresponding author✉: ricardo.carpio@unl.edu.ec.

Suggested citation: Carpio-Chilloallo, R and Paccha-Herrera, E. "Comparative study of cooling strategies in a lithium-ion battery module for thermal runaway prevention using CFD," *Ingenius, Revista de Ciencia y Tecnología*, N.º 33, pp. 76-90, 2025, DOI: <https://doi.org/10.17163/ings.n33.2025.07>.

1. Introduction

Lithium-ion batteries (LIBs) are essential components in a wide array of applications, including portable electronic devices, electric vehicles, smartphones, and medical equipment. Despite their widespread use, these batteries face critical challenges, particularly the need to prevent operation at elevated temperatures. Excessive heat can trigger thermal runaway, an uncontrolled exothermic reaction that poses serious risks, including fires that threaten human safety and compromise device integrity [1].

Lithium-ion batteries (LIBs) have emerged as a reliable energy source, renowned for their high efficiency, energy density, and relatively long lifespan [2]. A typical LIB cell comprises a negative electrode (graphite anode), a positive electrode (lithium metal oxide cathode), a separator, and an electrolyte. The separator is positioned between the electrodes to prevent electrical contact while permitting the passage of ions. The electrolyte facilitates ionic conduction within the cell [3]. The charge and discharge cycles of LIBs are defined by the transfer of lithium ions and electrons, a process known as ionization and oxidation [4].

The operation of LIBs is highly temperature-sensitive, with optimal and safe performance typically achieved within the range of 15 °C to 35 °C [5]. During cycling and usage, a material layer known as the solid electrolyte interface (SEI) forms on the surface of the electrodes. This layer begins to decompose at approximately 100 °C. Additionally, the separator material melts and shrinks at 143 °C. At temperatures exceeding 150 °C, thermal runaway, a hazardous and uncontrolled exothermic reaction, can occur [6–9].

Since their invention, lithium-ion batteries have undergone significant advancements in safety. However, the risk of fire and explosion persists due to the potential for thermal runaway. Thermal runaway occurs when the temperature within the battery rises exponentially, surpassing the system's ability to dissipate heat into the environment effectively. This excessive heat is generated by the exothermic chemical decomposition of materials within the cells [10].

Various cooling systems have been developed to ensure the battery operates within an appropriate temperature range. These systems are typically classified based on the cooling medium used, which may include air, liquid, or phase change material (PCM) [11, 12].

Air cooling systems can be classified into two types: natural air cooling and forced air cooling (using fans) [13, 14].

Liquid cooling systems for batteries can be classified as either direct or indirect. Direct cooling involves direct contact between the coolant and the battery cells. In contrast, indirect cooling entails immersing battery packs in an insulating coolant, such as mineral or silicone oils, which are chemically inert and do not

react with the materials on the cell surfaces [13].

Phase change material (PCM) cooling systems utilize substances that absorb or release substantial amounts of thermal energy during phase transitions, enabling heating or cooling as needed [15].

Numerous studies have investigated air, water, and PCM cooling systems to mitigate the risk of thermal runaway. For instance, Ouyang et al. [16] conducted experiments using one hundred 18650-type lithium-ion batteries and demonstrated that incorporating a 4 mm-thick layer of aerogel effectively reduces the maximum temperature of the batteries.

Zhou et al. [17] investigated a battery thermal management system (BTMS) incorporating heat pipes and phase change liquids to regulate temperature and prevent thermal propagation. Their results demonstrated that the system effectively mitigates overheating and thermal runaway, maintaining the battery temperature below 185 °C and limiting the temperature variation to less than 2.1 °C, even under high discharge rate conditions.

Alghamdi et al. [18] conducted an experimental study on various thermal management systems for LIBs in electric vehicles, focusing on the application of PCM. The findings revealed that using PCM alone results in an average temperature of 85 °C, exceeding the safe operational range. However, the incorporation of a thermoelectric module and aluminum fins significantly reduced the average temperature to 48 °C, enhancing the system's safety.

Wu et al. [19] developed a battery thermal management system (BTMS) for electric and hybrid vehicles, utilizing phase change materials (PCM) in combination with heat pipes. Experimental results indicated that the incorporation of heat pipes significantly improves temperature distribution under high discharge rates, maintaining the maximum temperature below 50 °C and achieving more stable thermal fluctuations during cyclic operation. Furthermore, the study demonstrated that a slight increase in airspeed further reduces cell temperatures, attributed to the PCM's phase transition process.

Liu et al. [20] conducted simulations to analyze thermal runaway behaviors in a pack of twelve prismatic LIBs and evaluated three thermal safety measures to mitigate internal short circuits. The study proposed using paraffin-based PCM to delay thermal runaway propagation between the batteries. Furthermore, the authors demonstrated that incorporating insulation into the PCM could further extend this delay. Additionally, a novel thermal protection method utilizing immersion cooling with boiling fluorinated liquid was introduced.

Li et al. [21] developed a numerical thermal abuse model using a Computational Fluid Dynamics (CFD) approach to investigate thermal propagation in lithium-ion battery packs. The model revealed that the spacing

between cells facilitates accelerated heat transfer; however, this design compromises energy density.

Numerous studies have focused on simulating the electrochemical-thermal coupling of batteries, a complex problem within the multiscale and multiphysics domain. To address this challenge, the multidimensional multiscale (MSMD) method has been employed and implemented in ANSYS Fluent. This approach solves equations at various scales and across multiple domains [22], enabling the simulation of battery packs with electrically connected cells [23]. Furthermore, the MSMD method can model thermal runaway in batteries under thermal abuse and short-circuit conditions [24]. Paccha-Herrera et al. [25] further advanced this approach by integrating the empirical NTGK model, which facilitates the calculation of thermal and electrical properties, thereby enhancing the assessment of the thermal performance of LIBs.

This study aims to analyze strategies for preventing thermal runaway by evaluating various cooling methods and geometric arrangements of cell models. The primary motivation is to mitigate the risk of thermal runaway in lithium-ion batteries when operating outside the prescribed temperature range, thereby reducing the likelihood of fires or explosions.

This study presents proposed solutions for prevent-

ing thermal runaway in lithium-ion batteries through the implementation of advanced cooling systems, using CFD-based analysis and simulation. Various geometric configurations of battery cells and cooling strategies are explored to enhance safety and efficiency. These findings aim to contribute to the development of safer and more reliable lithium-ion battery systems.

2. Materials and methods

This study employs three distinct geometric arrangements of battery cells with different cooling systems. Numerical simulations are conducted using the ANSYS STUDENT 2024 R1 software package, leveraging Computational Fluid Dynamics (CFD) models for detailed analysis.

Figure 1 provides a schematic representation of the methodology employed in this study to evaluate cooling strategies for preventing thermal runaway. The process begins with the selection of the battery cell and cooling systems. Next, geometries and meshing are developed. Subsequently, appropriate CFD models are chosen, and materials, initial and boundary conditions, and the numerical solver are configured. The procedure concludes with a comprehensive analysis of the simulation results.

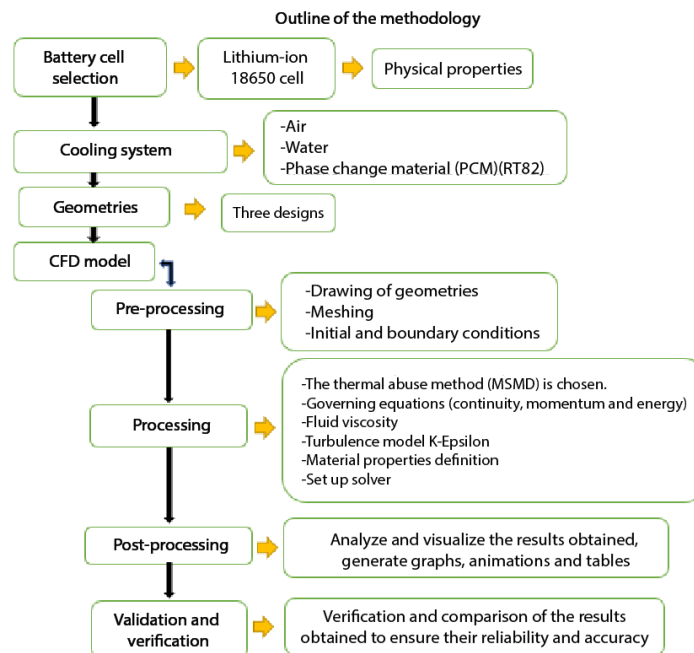


Figure 1. Schematic representation of the CFD study methodology for preventing thermal runaway

2.1. Numerical resolution

The governing equations utilized in the CFD simulations for the air and water domains include the continuity, momentum, and energy equations. The simulations

assume incompressible flow conditions, under which fluid density remains constant. The continuity equation is expressed as Equation (1) [26]:

$$\nabla \cdot \vec{v} = 0 \quad (1)$$

Where ∇ is the divergence operator and \vec{v} is the fluid velocity vector.

Equation (2) represents the momentum conservation equation for an incompressible, viscous fluid:

$$\frac{\partial \vec{v}}{\partial t} + (\vec{v} \cdot \nabla) \vec{v} = \frac{\nabla p}{\rho} + \frac{\mu}{\rho} \nabla^2 \vec{v} \quad (2)$$

Equation (3) illustrates the energy conservation equation for a fluid:

$$\frac{\partial(\rho e)}{\partial t} + \nabla(\rho e \vec{v}) = -p \nabla \cdot \vec{v} + \nabla \cdot (k_f \nabla T) + \Phi \quad (3)$$

Where \vec{v} is the fluid velocity, p is the pressure, ρ is the air density, μ is the dynamic viscosity, e is the internal energy, T is the temperature, k_f is the thermal conductivity of the fluid, Φ is the viscous dissipation, and t is time.

To model the effects of turbulence, the $k - \epsilon$ model was used due to its robustness [27].

In the case of PCM RT82, where a phase change occurs, the continuity equation (Equation (4)), momentum equation (Equation (5)), and energy equation (Equation (6)) are applied [28].

$$\frac{\partial(\rho_f)}{\partial t} + \nabla \cdot (\rho_f \vec{U}) = 0 \quad (4)$$

Where $\frac{\partial \rho_f}{\partial t}$ is the rate of temporal change of density, ρ_f is the fluid phase density, and \vec{U} is the fluid velocity vector (with components \vec{u} , \vec{v} and \vec{w}).

$$\rho_f \frac{\partial \vec{U}}{\partial t} + \rho_f (\vec{U} \cdot \nabla) \vec{U} = -\nabla p + \mu \nabla^2 \vec{U} + \frac{(1 - f_l)^2}{f_l^3 + \delta} A_m \vec{U} + \rho_f g \beta (T_f - T_m) \vec{k} \quad (5)$$

Where β is the consecutive number in the transition region (mushy region), A_m is a parameter for the transition region, δ is a small value introduced to prevent division by zero, and f_l is the liquid fraction.

$$\frac{\partial \rho_f H_f}{\partial t} + \nabla \cdot (\rho_f \vec{u} H_f) = k_f \nabla^2 T_f \quad (6)$$

Where H_f is the fluid enthalpy.

2.2. NTGK model

The thermal runaway phenomenon was modeled using Multiscale Multidomain Modeling (MSMD), based on the empirical NTGK/DCIR model.

The NTGK model, described by Equations (7), (8) and (9), enables the calculation of the thermoelectric properties of the anode, cathode, and active zone domains within a cell or electrically connected battery pack [25]:

$$\frac{\partial(\rho C_p T)}{\partial t} - \nabla \cdot (k_c \nabla T) = \sigma_{\text{pos}} |\nabla \phi_{\text{pos}}|^2 + \sigma_{\text{gen}} |\nabla \phi_{\text{neg}}|^2 + q_{\text{ech}} \quad (7)$$

$$\nabla \cdot (\sigma_{\text{pos}} \nabla \phi_{\text{pos}}) = -j \quad (8)$$

$$\nabla \cdot (\sigma_{\text{neg}} \nabla \phi_{\text{neg}}) = -j \quad (9)$$

Where k_c is the thermal conductivity, σ is the electrical conductivity, ϕ is the electric potential, q_{ech} is the heat transfer rate resulting from thermal exchange with the environment, and the subscripts "pos" and "neg" refer to the positive and negative electrodes, respectively. The volumetric current density j is defined by Equation (10) [29]:

$$j = \frac{C_N}{C_{\text{ref}} \text{Vol}} Y [U - (\phi_{\text{pos}} - \phi_{\text{neg}})] \quad (10)$$

Where Vol is the volume of the active zone, C_{ref} is the battery capacity used to derive the parameters for the functions U and Y , which are defined by Equations (11) and (12), respectively [29]. The corresponding coefficients for these functions are presented in Table 1.

$$U = \left(\sum_{n=0}^5 a_n (D0D)^n \right) - C_2 (T - T_{\text{ref}}) \quad (11)$$

$$Y = \left(\sum_{n=0}^5 b_n (D0D)^n \right) \exp \left[-C_1 \left(\frac{1}{T} - \frac{1}{T_{\text{ref}}} \right) \right] \quad (12)$$

Where C_2 and C_1 are constants for a specific battery.

Table 1. Parámetros para el modelo NTGK [25]

Funciones	
U	Y
$a_0=4.0682$	$b_0=16.5066$
$a_1=-1.2669$	$b_1=-27.0367$
$a_2=-0.9072$	$b_2=237.3297$
$a_3=3.7550$	$b_3=-632.603$
$a_4=-2.3108$	$b_4=725.0825$
$a_5=-0.1701$	$b_5=-309.8760$

The heat transfer rate resulting from thermal exchange with the environment q_{ech} is defined by Equation (13) [25]:

$$q_{\text{ech}} = j \left[U - (\phi_{\text{pos}} - \phi_{\text{neg}}) - T \frac{dU}{dT} \right] \quad (13)$$

Where the first term represents the overpotential heat, and the second term corresponds to the entropic component.

2.3. Thermal abuse model

The thermal abuse model was initially proposed by Harchard et al. [30] and subsequently expanded by Kim et al. [31]. This model is based on the Arrhenius equation and includes a system of equations that describe the reactions occurring during the decomposition of the positive electrode, the negative electrode, and the solid-electrolyte interface (SEI), as outlined below:

$$\frac{dc_{sei}}{dt} = -c_{sei}A_{sei} \cdot \exp\left(-\frac{E_{a,sei}}{RT}\right) \quad (14)$$

$$\frac{dc_{ne}}{dt} = -c_{ne}A_{ne} \cdot \exp\left(-\frac{z_{sei}}{z_{sei,0}}\right) \cdot \exp\left(-\frac{E_{a,ne}}{RT}\right) \quad (15)$$

$$\frac{dz_{sei}}{dt} = c_{ne}A_{ne} \cdot \exp\left(-\frac{z_{sei}}{z_{sei,0}}\right) \cdot \exp\left(-\frac{E_{a,ne}}{RT}\right) \quad (16)$$

$$\frac{d\alpha}{dt} = \alpha(1 - \alpha)A_{pe} \cdot \exp\left(-\frac{E_{a,pe}}{RT}\right) \quad (17)$$

$$\frac{dc_{el}}{dt} = -c_{el}A_{el} \cdot \exp\left(-\frac{E_{a,el}}{RT}\right) \quad (18)$$

Where the subscripts *ne*, *np* and *el* represent the reaction between the negative electrode and the electrolyte, the reaction between the positive electrode and the electrolyte, and the decomposition reaction of the electrolyte, respectively. Additionally, z_{sei} is a dimensionless measure of the SEI layer thickness; $z_{(sei,0)}$ is the reference thickness of the SEI layer; c_{sei} is the fraction of the concentration of metastable lithium-containing species in the SEI layer; c_{ne} is the fraction of the lithium concentration in the negative electrode; α represents the conversion degree of the cathode, and c_{el} is the concentration of the electrolyte. All these variables are dimensionless. R is the universal gas constant.

2.4. Battery Cell Selection

In this study, 18650-type cylindrical lithium-ion cells were used. The properties are detailed in Table 2.

Table 2. Properties of the 18650 lithium-ion cell [26]

Parameters	Units	Value
Diameter	mm	18.4
Height	mm	65
Nominal capacity	Ah	2.15
Nominal voltage	V	3.62
Maximum charge rate	-	1 C
Maximum discharge rate	-	4.65 C
Internal resistance	$m \cdot \Omega$	35
Density	kg/m^3	1852
Heat capacity	$J/kg \cdot K$	1200
Thermal conductivity	-	-
Axial	$W/m \cdot K$	0.2
Radial	$W/m \cdot K$	37.6

Figure 2 illustrates the main components of the 18650 lithium-ion battery used in this study. The battery features a diameter of 18.4 mm, an anode height of 2 mm, a cathode height of 3 mm, and an active zone of 60 mm.

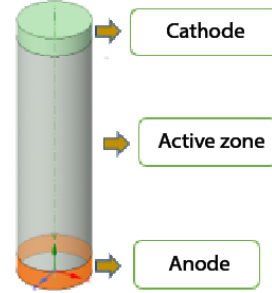


Figure 2. Main components of a lithium-ion battery used in the MSMD approach

2.5. Cooling systems

The cooling systems proposed in this study include air, water, and PCM. For the PCM, RT82 is employed, which consists of pure organic materials capable of storing and releasing significant amounts of heat through a solid-to-liquid or liquid-to-solid phase change process [32]. The properties of the RT82 PCM are detailed in Table 3.

Table 3. Properties of the RT82 PCM [32]

Thermophysical properties	Units	Value
Density (solid)	$kg \cdot m^{-3}$	950
Density (liquid)	$kg \cdot m^{-3}$	770
Specific heat	$J \cdot (kg^{-1} \cdot K^{-1})$	2000
Thermal conductivity	$W \cdot (m^{-1} \cdot K^{-1})$	0.2
Latent heat	J/kg	176000
Dynamic viscosity	$kg/m \cdot s$	0.03499
Temperature (solid)	K	350.15
Temperature (liquid)	K	358.15
Thermal expansion coefficient	1/K	0.001

2.6. Geometric arrangements of the cells

The geometries used in this study were designed using the Ansys Space Claim module within ANSYS Fluent.

Three geometries, each consisting of sixteen 18650 lithium-ion cells, were proposed with varying arrangements, using three different cooling methods: air, water, and PCM RT82. The thermal runaway behavior of the cells was analyzed using the thermal abuse model in ANSYS Fluent, which is based on the Multiscale Multidomain (MSMD) method and incorporates the empirical NTGK model.

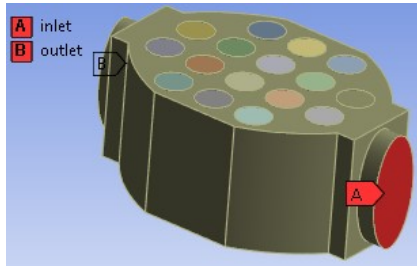


Figure 8. Geometry 2: Coolant flow

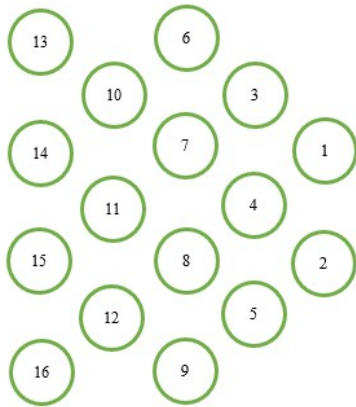


Figure 9. Cell arrangement for Geometry 3

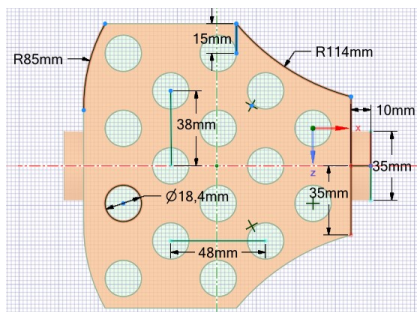


Figure 10. Geometry 3: Dimensions

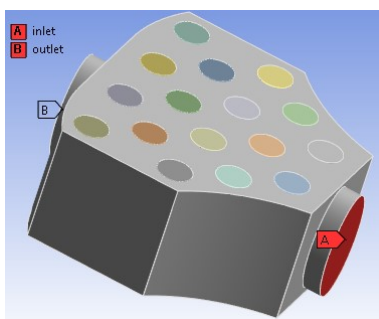


Figure 11. Geometry 3: Coolant flow

3. Results and discussion

Figure 12 presents a representative graph illustrating the cooling process of a cell using air, demonstrating that steady-state conditions are achieved by the end of the process.

Figure 13 illustrates a typical pattern of thermal runaway, where a minor temperature increase after 505 seconds triggers an uncontrolled chain reaction, resulting in an exponential rise in the system's temperature. This phenomenon is particularly critical in lithium-ion batteries, as it can lead to catastrophic failures if not effectively managed.

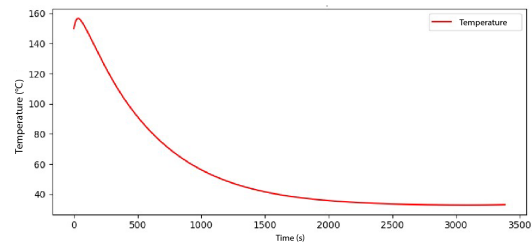


Figure 12. Cooling dynamics of a battery. Air cooling with forced convection, ambient and inlet temperature of 25°C, and inlet velocity of $1.5 \frac{m}{s}$

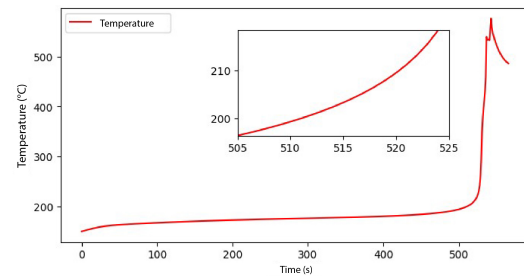


Figure 13. Characteristic temperature profile of thermal runaway in a cell. Air cooling, with an inlet temperature to the module of 47°C and velocity of $1.5 \frac{m}{s}$

3.1. Air cooling

Figure 14 illustrates the temperature profiles of the cells in Geometry 1 under natural convection air cooling. This method fails to prevent thermal runaway, with Cell 16 being the first to exhibit this phenomenon at 258 seconds. Figure 15 depicts the temperature distribution across the cells.

Figure 16 presents the results for Geometry 2 with natural convection air cooling, which fails to prevent thermal runaway. Cells 15 and 16 are the first to exhibit this abnormal condition, occurring after 228 seconds. The temperature distribution across the cells is depicted in Figure 17.

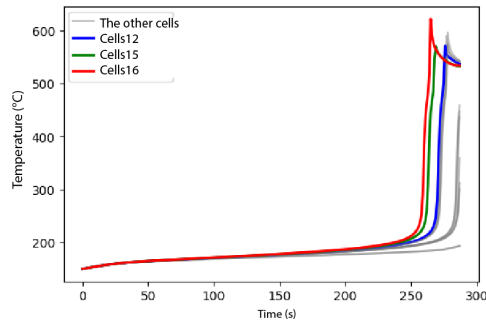


Figure 14. Geometry 1. Air cooling under natural convection

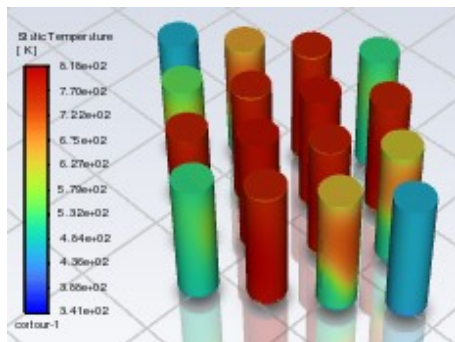


Figure 15. Geometry 1. Cell temperature at 287 s through natural air convection

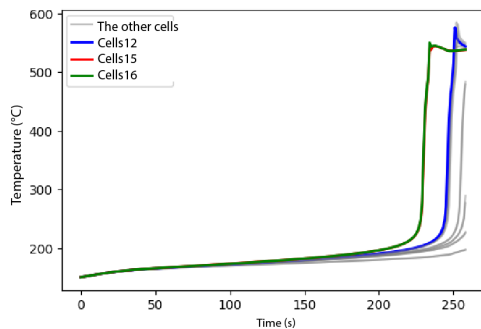


Figure 16. Geometry 2. Air cooling under natural convection

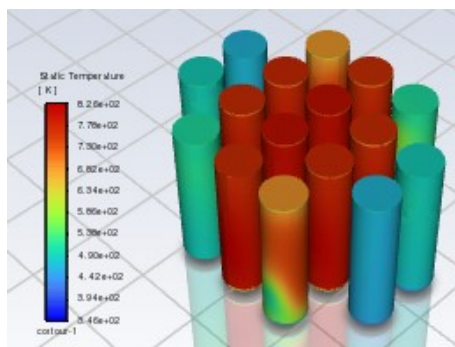


Figure 17. Geometry 2. Cell temperature at 258 s through natural air convection

Figure 18 illustrates the battery temperature profiles for Geometry 3 under natural convection air cooling, with Cell 15 being the first to undergo thermal runaway after 255 seconds. The temperature distribution across the cells is more clearly depicted in Figure 19, highlighting that the central cells experience the most significant temperature increases.

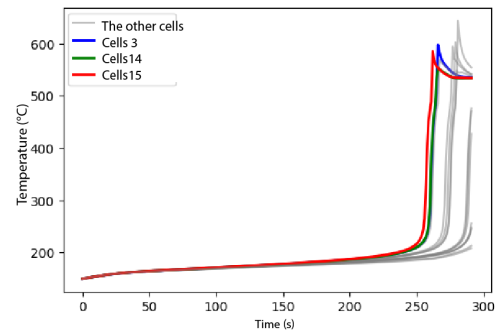


Figure 18. Geometry 3. Air cooling through natural convection

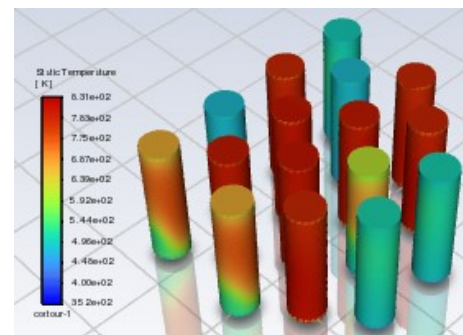


Figure 19. Geometry 3. Cell temperature at 292 s through natural air convection

Figure 20 illustrates the temperature curves for Geometry 1 under forced convection air cooling, which successfully prevents thermal runaway. Cell 5 reaches the highest temperature of 156.98°C within 35 seconds. Figure 21 depicts the temperature distribution across the cells, highlighting insufficient cooling in the cells located at the extremes.

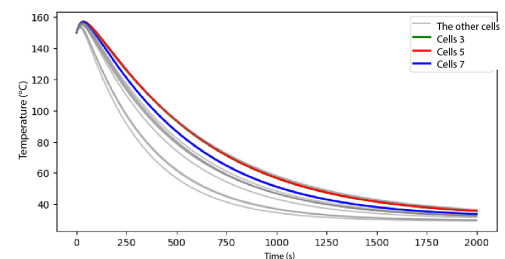


Figure 20. Geometry 1. Forced air convection

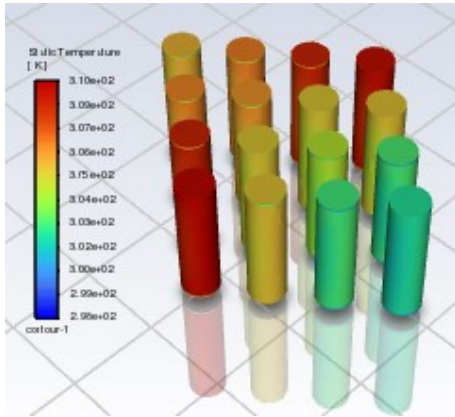


Figure 21. Geometry 1. Cell temperature at 2000 s through forced air convection

Figure 22 presents the temperature evolution of the cells for Geometry 2 under forced convection air cooling, which effectively inhibits thermal runaway. Cell 3 reaches the highest temperature of 157.30°C within 33 seconds. Figure 23 depicts the temperature distribution within the module, indicating that cells located near the air inlet are better cooled compared to those positioned near the air outlet.

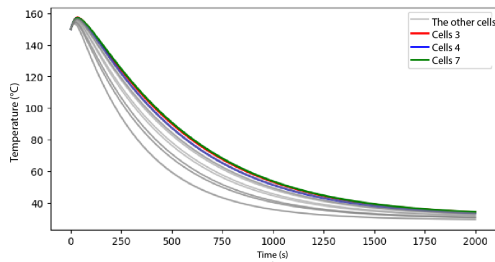


Figure 22. Geometry 2. Forced air convection

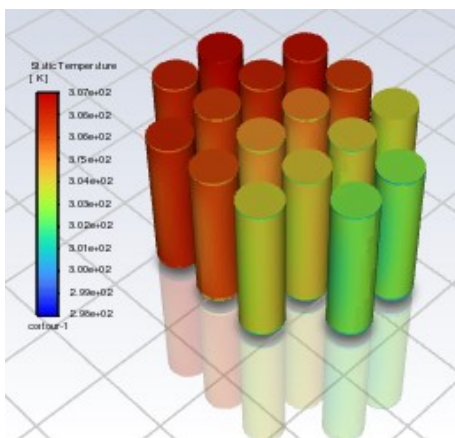


Figure 23. Geometry 2. Cell temperature at 2000 s through forced air convection

Figure 24 illustrates the results for Geometry 3 under forced convection air cooling, which successfully

prevents thermal runaway. However, a greater temperature gradient is observed between neighboring cells compared to Geometry 2. Cell 13 reaches the highest temperature of 159.31°C within 56 seconds. Figure 25 depicts the temperature distribution across the cells, showing that those in the central zone of the module benefit from better cooling.

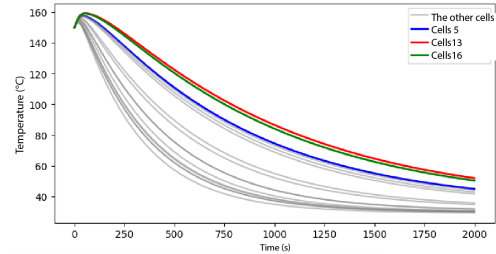


Figure 24. Geometry 3. Forced air convection

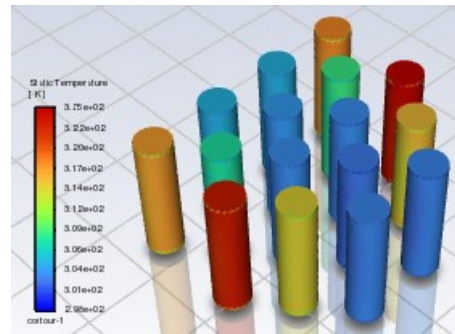


Figure 25. Geometry 3. Cell temperature at 2000 s through forced air convection

3.2. Water cooling

Figure 26 depicts the temperature decay of the cells in Geometry 1, with water cooling via natural convection successfully inhibiting thermal runaway. Cell 16 reaches the highest temperature of 155.90°C within 27 seconds. Figure 27 illustrates the temperature distribution across the cells, demonstrating an almost uniform temperature profile.

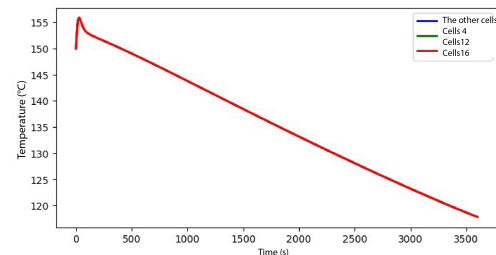


Figure 26. Geometry 1. Water cooling with natural convection

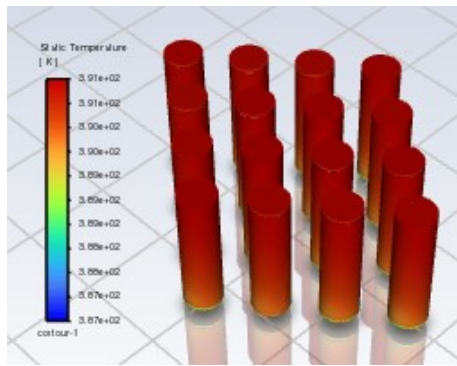


Figure 27. Geometry 1. Cell temperature at 3600 s through natural water convection

Figure 28 illustrates the thermal behavior of the cells in Geometry 2 under water cooling via natural convection, which effectively prevents thermal runaway. Cell 16 reaches the highest temperature of 156.09°C within 29 seconds. Figure 29 shows the temperature distribution across the cells, demonstrating a uniform profile.

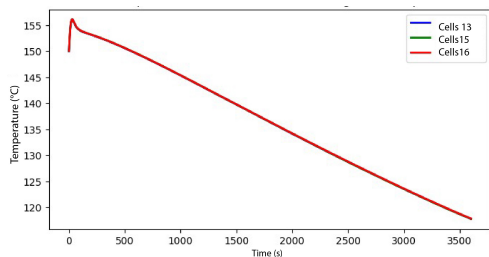


Figure 28. Geometry 2. Water cooling through natural convection

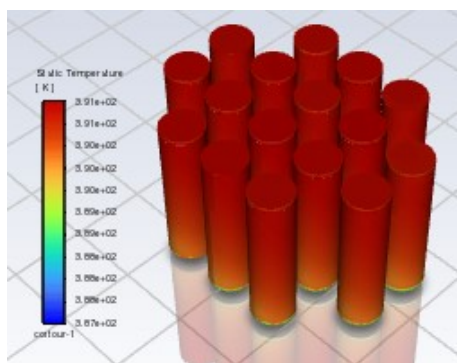


Figure 29. Geometry 2. Cell temperature at 3600 s through natural water convection

Figure 30 presents the results for Geometry 3 with water cooling via natural convection. Cell 7 reaches the highest temperature of 156.19°C within 29 seconds, with no occurrence of thermal runaway. Figure 31 illustrates the uniform temperature distribution across the batteries.

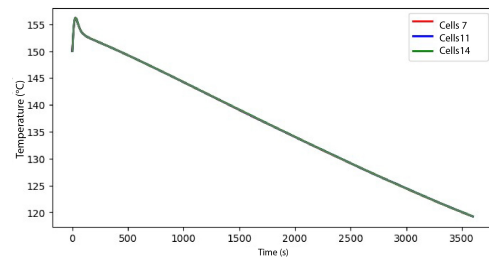


Figure 30. Geometry 3. Water cooling with natural convection

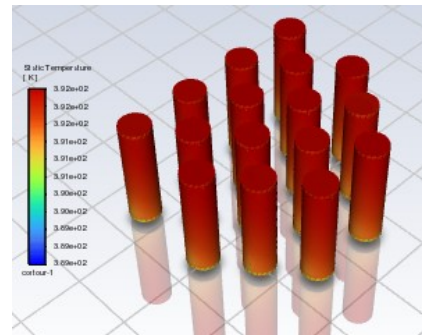


Figure 31. Geometry 3. Cell temperature at 3600 s through natural water convection

Figure 32 illustrates the temperature profiles of selected cells in Geometry 1 with water cooling via forced convection. All cells reach a steady-state condition, effectively inhibiting thermal runaway. Figure 33 depicts a uniform temperature distribution across the cells.

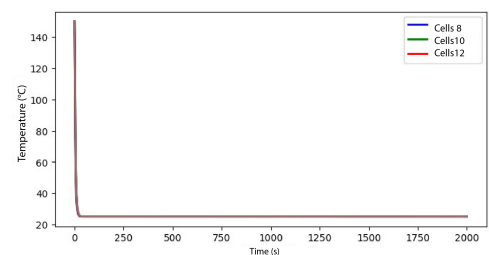


Figure 32. Geometry 1. Water cooling via forced convection

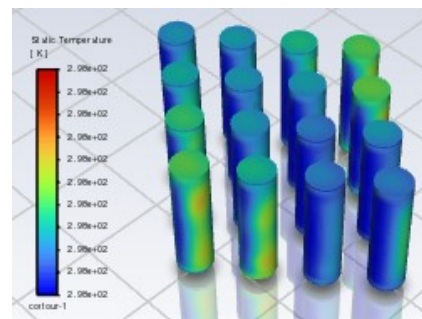


Figure 33. Geometry 1. Cell temperature at 2000 s through forced water convection

Figure 34 illustrates the cell temperature profiles for Geometry 2 with water cooling via forced convection. This cooling method effectively prevents thermal runaway, allowing the system to reach a steady-state condition.

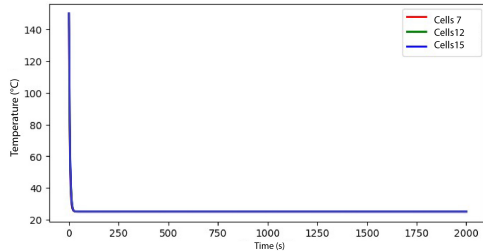


Figure 34. Geometry 2. Water cooling via forced convection

Figure 35 depicts the temperature distribution across the cells, demonstrating a uniform pattern.

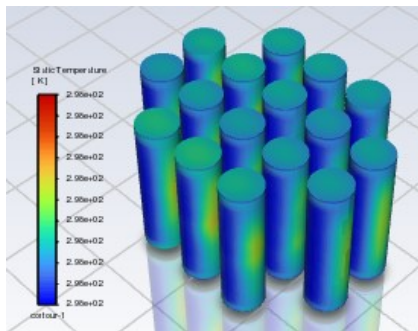


Figure 35. Geometry 2. Cell temperature at 2000 s through forced water convection

Figure 36 presents the results for Geometry 3 with water cooling via forced convection. In this scenario, thermal runaway is effectively inhibited, and a steady-state condition is achieved.

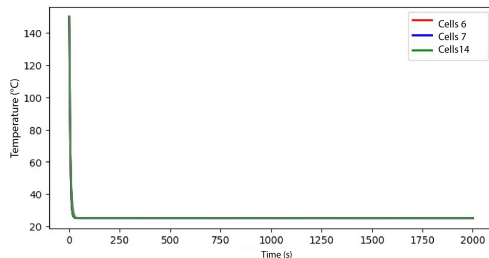


Figure 36. Geometry 3. Water cooling, forced convection

Figure 37 illustrates the temperature distribution across the cells, highlighting negligible temperature gradients.

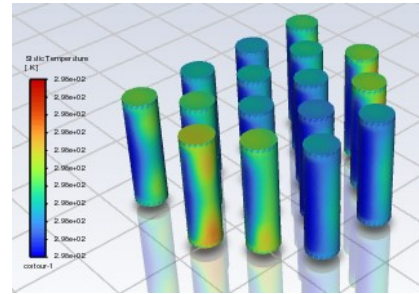


Figure 37. Geometry 2. Cell temperature at 2000 s through forced water convection

3.3. Cooling by PCM (RT82)

Figure 38 illustrates the thermal behavior of Geometry 1 with cooling with PCM (RT82), which successfully prevents thermal runaway. Cell 16 reaches the highest temperature of 161.40°C within 61 seconds, followed by a temperature decay. Figure 39 depicts a uniform temperature distribution across the cells.

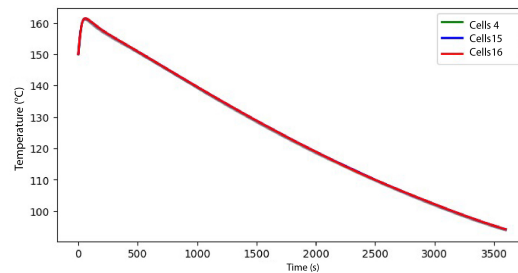


Figure 38. Geometry 1. Cooling by PCM (RT82)

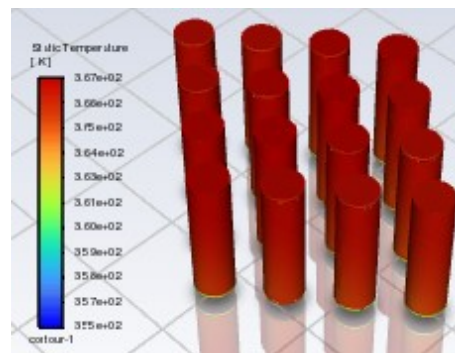


Figure 39. Geometry 1. Cell temperature at 3600 s, cooled by PCM (RT82)

Figure 40 illustrates the cell temperature profiles for Geometry 2 using cooling with PCM (RT82). In this case, thermal runaway is also effectively prevented, with Cells 15 and 16 reaching the highest temperature of 161.71°C within 74 seconds. Figure 41 depicts the temperature distribution across the cells, demonstrating a uniform pattern.

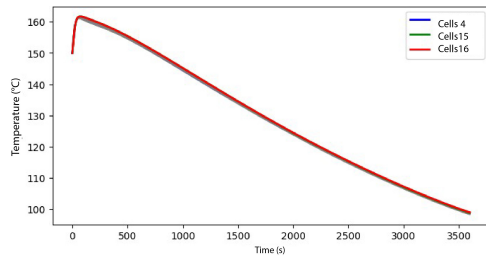


Figure 40. Geometry 2. Cooling by PCM (RT82)

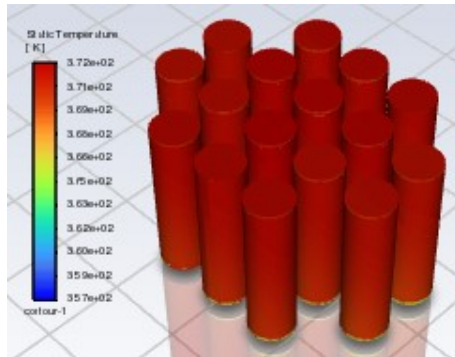


Figure 41. Geometry 2. Cell temperature at 3600 s, cooled by PCM (RT82)

Figure 42 presents the results for Geometry 3 using cooling with PCM. Cell 15 reaches the highest temperature of 161.46°C within 59 seconds, followed by a temperature decay.

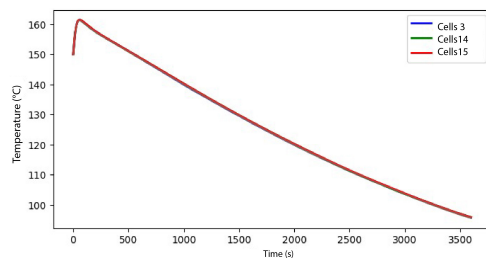


Figure 42. Geometry 3. Cooling by PCM (RT82)

Figure 43 illustrates that the temperature distribution across the cells remains uniform, consistent with the other geometric configurations using PCM.

The phenomenon of thermal runaway plays a critical role in selecting the cooling system and geometric arrangement of battery cells, as its mitigation is highly dependent on these parameters. Consequently, numerous studies have addressed this issue. For instance, Zhou et al. [17] successfully prevented the propagation of thermal runaway, maintaining the temperature below 185°C, with temperatures exceeding 60°C for only 14 seconds. Similarly, Ouyang et al. [16] reduced the maximum temperature of 18650-type batteries from 740.35°C to 55.19°C, effectively preventing thermal runaway. In another study, Alghamdi et al. [18]

employed paraffin-based PCM, achieving an average temperature of 85°C.

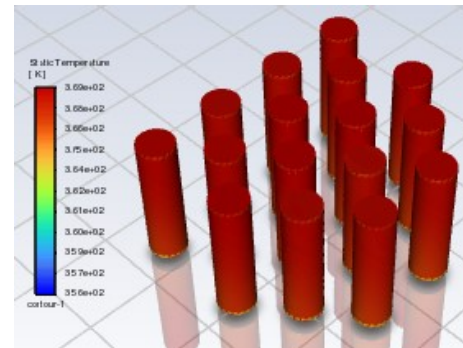


Figure 43. Geometry 3. Cell temperature at 3600 s, cooled by PCM (RT82)

4. Conclusions

A numerical study was conducted to analyze the cooling performance of battery cells within a module utilizing air, water, and phase change material (PCM) as cooling methods. Three distinct geometric configurations of the battery module were proposed to evaluate their effectiveness in inhibiting thermal runaway.

Among the geometries analyzed, none of the three configurations successfully prevented thermal runaway when cooled using natural air convection. However, the phenomenon was effectively inhibited when water and PCM RT82 were employed as the cooling medium. For water cooling, Geometry 1 proved to be the most efficient, with a maximum temperature of 155.90°C. Similarly, when PCM RT82 was used, Geometry 1 also demonstrated the best performance, reaching a maximum temperature of 161.40°C.

Using forced air convection, Geometry 1 emerged as the most efficient configuration, achieving a maximum temperature of 156.98°C. Similarly, with water cooling, Geometry 1 demonstrated superior performance, effectively reducing the temperature from 150°C to 25.06°C.

Based on the results obtained, it can be concluded that Geometry 1 is the most efficient configuration for thermal management in the studied scenarios.

Among the three cooling systems analyzed in this study, water proved to be the most efficient in preventing thermal runaway. This efficiency is attributed to its high heat capacity and thermal conductivity, which enable effective heat distribution and dissipation.

A key limitation of this study is the limited number of cells analyzed. To address this, future work should incorporate models with more diverse geometric configurations and a larger number of cells to improve the robustness of the findings. Additionally, future research should evaluate the effects of indirect contact between

cells and the coolant, as well as explore alternative types of phase change materials (PCM).

This study provides valuable insights into the thermal runaway phenomenon, aiding in the development of more effective cooling systems to prevent it.

References

- [1] R. Gebart, “Thermal runaway criterion for thick polymer composites,” *Composites Part A: Applied Science and Manufacturing*, vol. 182, p. 108187, 2024. [Online]. Available: <https://doi.org/10.1016/j.compositesa.2024.108187>
- [2] A. M. Divakaran, D. Hamilton, K. N. Manjunatha, and M. Minakshi, “Design, development and thermal analysis of reusable li-ion battery module for future mobile and stationary applications,” *Energies*, vol. 13, no. 6, 2020. [Online]. Available: <https://doi.org/10.3390/en13061477>
- [3] G. E. Blomgren, “The development and future of lithium ion batteries,” *Journal of The Electrochemical Society*, vol. 164, no. 1, p. A5019, dec 2016. [Online]. Available: <https://dx.doi.org/10.1149/2.0251701jes>
- [4] A. Carnovale, *Investigation into the Effect of Thermal Management on the Capacity Fade of Lithium-ion Batteries*. Mechanical and Mechatronics Engineering. University of Waterloo, 2016. [Online]. Available: <https://upsalesiana.ec/ing33ar6r4>
- [5] D. Patel, J. B. Robinson, S. Ball, D. J. L. Brett, and P. R. Shearing, “Thermal runaway of a li-ion battery studied by combined arc and multi-length scale x-ray ct,” *Journal of The Electrochemical Society*, vol. 167, no. 9, p. 090511, apr 2020. [Online]. Available: <https://dx.doi.org/10.1149/1945-7111/ab7fb6>
- [6] G. Guo, B. Long, B. Cheng, S. Zhou, P. Xu, and B. Cao, “Three-dimensional thermal finite element modeling of lithium-ion battery in thermal abuse application,” *Journal of Power Sources*, vol. 195, no. 8, pp. 2393–2398, 2010. [Online]. Available: <https://doi.org/10.1016/j.jpowsour.2009.10.090>
- [7] J. Fan, “On the discharge capability and its limiting factors of commercial 18650 li-ion cell at low temperatures,” *Journal of Power Sources*, vol. 117, no. 1, pp. 170–178, 2003. [Online]. Available: [https://doi.org/10.1016/S0378-7753\(03\)00354-9](https://doi.org/10.1016/S0378-7753(03)00354-9)
- [8] K. Amin, J. Zhang, H.-Y. Zhou, R. Lu, M. Zhang, N. Ashraf, C. YueLi, L. Mao, C. F. J. Faul, and Z. Wei, “Surface controlled pseudo-capacitive reactions enabling ultra-fast charging and long-life organic lithium ion batteries,” *Sustainable Energy Fuels*, vol. 4, pp. 4179–4185, 2020. [Online]. Available: <http://dx.doi.org/10.1039/D0SE00610F>
- [9] K. Märker, C. Xu, and C. P. Grey, “Operando nmr of nmc811/graphite lithium-ion batteries: Structure, dynamics, and lithium metal deposition,” *Journal of the American Chemical Society*, vol. 142, no. 41, pp. 17 447–17 456, Oct 2020. [Online]. Available: <https://doi.org/10.1021/jacs.0c06727>
- [10] R. D. McKerracher, J. Guzman-Guemez, R. G. A. Wills, S. M. Sharkh, and D. Kramer, “Advances in prevention of thermal runaway in lithium-ion batteries,” *Advanced Energy and Sustainability Research*, vol. 2, no. 5, p. 2000059, 2021. [Online]. Available: <https://doi.org/10.1002/aesr.202000059>
- [11] Z. Rao and S. Wang, “A review of power battery thermal energy management,” *Renewable and Sustainable Energy Reviews*, vol. 15, no. 9, pp. 4554–4571, 2011. [Online]. Available: <https://doi.org/10.1016/j.rser.2011.07.096>
- [12] H. Behi, D. Karimi, R. Youssef, M. Suresh Patil, J. Van Mierlo, and M. Bercibar, “Comprehensive passive thermal management systems for electric vehicles,” *Energies*, vol. 14, no. 13, 2021. [Online]. Available: <https://doi.org/10.3390/en14133881>
- [13] T. I. C. Buidin and F. Mariasiu, “Battery thermal management systems: Current status and design approach of cooling technologies,” *Energies*, vol. 14, no. 16, 2021. [Online]. Available: <https://doi.org/10.3390/en14164879>
- [14] J. Du, Y. Sun, Y. Huang, and X. Wu, “Analysis of influencing factors of thermal management system for lifepo4 lithium battery under high power charging,” *World Electric Vehicle Journal*, vol. 11, no. 2, 2020. [Online]. Available: <https://doi.org/10.3390/wevj11020044>
- [15] E. Grimonia, M. R. C. Andhika, M. F. N. Aulady, R. V. C. Rubi, and N. L. Hamidah, “Thermal management system using phase change material for lithium-ion battery,” *Journal of Physics: Conference Series*, vol. 2117, no. 1, p. 012005, nov 2021. [Online]. Available: <https://dx.doi.org/10.1088/1742-6596/2117/1/012005>
- [16] T. Ouyang, B. Liu, C. Wang, J. Ye, and S. Liu, “Novel hybrid thermal management system for preventing li-ion battery thermal runaway using nanofluids cooling,” *International Journal of Heat and Mass Transfer*, vol. 201, p. 123652, 2023. [Online]. Available: <https://doi.org/10.1016/j.ijheatmasstransfer.2022.123652>

- [17] H. Zhou, C. Dai, Y. Liu, X. Fu, and Y. Du, "Experimental investigation of battery thermal management and safety with heat pipe and immersion phase change liquid," *Journal of Power Sources*, vol. 473, p. 228545, 2020. [Online]. Available: <https://doi.org/10.1016/j.jpowsour.2020.228545>
- [18] H. Alghamdi, M. F. M. Rosdi, A. Mukhtar, A. S. H. M. Yasir, and A. Alviz-Meza, "Controlling thermal runaway by simultaneous use of thermoelectric module and phase change material in the lithium-ion batteries of electric vehicles," *Case Studies in Thermal Engineering*, vol. 52, p. 103697, 2023. [Online]. Available: <https://doi.org/10.1016/j.csite.2023.103697>
- [19] W. Wu, X. Yang, G. Zhang, K. Chen, and S. Wang, "Experimental investigation on the thermal performance of heat pipe-assisted phase change material based battery thermal management system," *Energy Conversion and Management*, vol. 138, pp. 486–492, 2017. [Online]. Available: <https://doi.org/10.1016/j.enconman.2017.02.022>
- [20] X. Liu, Z. Zhou, W.-T. Wu, L. Wei, W. Wu, Y. Li, L. Gao, Y. Li, and Y. Song, "Modelling for the mitigation of lithium ion battery thermal runaway propagation by using phase change material or liquid immersion cooling," *Case Studies in Thermal Engineering*, vol. 52, p. 103749, 2023. [Online]. Available: <https://doi.org/10.1016/j.csite.2023.103749>
- [21] Y. Li, G. Liu, and Z. Li, "Numerical modeling of thermal runaway in high-energy lithium-ion battery packs induced by multipoint heating," *Case Studies in Thermal Engineering*, vol. 38, p. 102335, 2022. [Online]. Available: <https://doi.org/10.1016/j.csite.2022.102335>
- [22] R. Ni, D. Zhang, R. Wang, Z. Xie, and Y. Wang, "Prevention and suppression effects of phase change material on thermal runaway in batteries," *Case Studies in Thermal Engineering*, vol. 48, p. 103160, 2023. [Online]. Available: <https://doi.org/10.1016/j.csite.2023.103160>
- [23] Y. Liu, Y. G. Liao, and M.-C. Lai, "Transient temperature distributions on lithium-ion polymer sli battery," *Vehicles*, vol. 1, no. 1, pp. 127–137, 2019. [Online]. Available: <https://doi.org/10.3390/vehicles1010008>
- [24] Q. Li, C. Yang, S. Santhanagopalan, K. Smith, J. Lamb, L. A. Steele, and L. Torres-Castro, "Numerical investigation of thermal runaway mitigation through a passive thermal management system," *Journal of Power Sources*, vol. 429, pp. 80–88, 2019. [Online]. Available: <https://doi.org/10.1016/j.jpowsour.2019.04.091>
- [25] E. Paccha-Herrera, W. R. Calderón-Muñoz, M. Orchard, F. Jaramillo, and K. Medjaher, "Thermal modeling approaches for a licoo2 lithium-ion battery—a comparative study with experimental validation," *Batteries*, vol. 6, no. 3, 2020. [Online]. Available: <https://doi.org/10.3390/batteries6030040>
- [26] E. Paccha-Herrera, A. Medina-Sisalima, D. Tapiaperalta, B. Solórzano-Castillo, J. Gómez-Peña, and I. Coronel-Villavicencio, "A numerical study on the influence of geometric cell configurations over the thermal performance in a lithium-ion battery module," *IOP Conference Series: Earth and Environmental Science*, vol. 1370, no. 1, p. 012002, jul 2024. [Online]. Available: <https://dx.doi.org/10.1088/1755-1315/1370/1/012002>
- [27] B. Launder and D. Spalding, "The numerical computation of turbulent flows," *Computer Methods in Applied Mechanics and Engineering*, vol. 3, no. 2, pp. 269–289, 1974. [Online]. Available: [https://doi.org/10.1016/0045-7825\(74\)90029-2](https://doi.org/10.1016/0045-7825(74)90029-2)
- [28] H. Liu, C. Jin, H. Li, and Y. Ji, "A numerical study of pcm battery thermal management performance enhancement with fin structures," *Energy Reports*, vol. 9, pp. 1793–1802, 2023, selected papers from 2022 International Conference on Frontiers of Energy and Environment Engineering. [Online]. Available: <https://doi.org/10.1016/j.egyrs.2023.04.214>
- [29] K. H. Kwon, C. B. Shin, T. H. Kang, and C.-S. Kim, "A two-dimensional modeling of a lithium-polymer battery," *Journal of Power Sources*, vol. 163, no. 1, pp. 151–157, 2006, special issue including selected papers presented at the Second International Conference on Polymer Batteries and Fuel Cells together with regular papers. [Online]. Available: <https://doi.org/10.1016/j.jpowsour.2006.03.012>
- [30] T. D. Hatchard, D. D. MacNeil, A. Basu, and J. R. Dahn, "Thermal model of cylindrical and prismatic lithium-ion cells," *Journal of The Electrochemical Society*, vol. 148, no. 7, p. A755, jun 2001. [Online]. Available: <https://dx.doi.org/10.1149/1.1377592>
- [31] G.-H. Kim, A. Pesaran, and R. Spotnitz, "A three-dimensional thermal abuse model for lithium-ion cells," *Journal of Power Sources*, vol. 170, no. 2, pp. 476–489, 2007. [Online]. Available: <https://doi.org/10.1016/j.jpowsour.2007.04.018>
- [32] Y. Han, Y. Yang, T. Mallick, and C. Wen, "Nanoparticles to enhance melting performance of phase change materials

for thermal energy storage,” *Nanomaterials*,
vol. 12, no. 11, 2022. [Online]. Available:

<https://doi.org/10.3390/nano12111864>